Article

An Operando Investigation of Mn3O4+# Co-catalyst on Fe2O3 Photoanode: Mn-Valency Determined Enhancement at Varied Potentials

Ying Liu, Chao Wei, Chee Keong Ngaw, Ye Zhou, Shengnan Sun, Shibo Xi, Yonghua Du, Say Chye Joachim Loo, Joel W. Ager, and Zhichuan J. Xu

An Operando Investigation of $Mn_3O_{4+\delta}$ Co-catalyst on Fe_2O_3 Photoanode: Mn-Valency Determined Enhancement at Varied Potentials

Ying Liu,[†,Δ] Chao Wei,[†,Δ] Chee Keong Ngaw,[†] Ye Zhou,[†] Shengnan Sun,[†] Shibo Xi,[‡] Yonghua Du,[‡] Joachim S. C. Loo,*[,†,§] Joel W. Ager III,*[,⊥] and Zhichuan J. Xu*[,†,§,¶]

[†]School of Materials Science and Engineering, Nanyang Technological University, 50 Nanyang Avenue, 639798, Singapore

[‡]Institute of Chemical and Engineering Sciences, A*STAR, 1 Pesek Road, 627833, Singapore

[§]Solar Fuels Lab, Nanyang Technological University, 50 Nanyang Avenue, 639798, Singapore

[⊥]Department of Materials Science and Engineering, University of California at Berkeley, Berkeley, California 94720, USA

[¶]Energy Research Institute@NTU, Nanyang Technological University, 50 Nanyang Avenue, 639798, Singapore.

ABSTRACT: The development of efficient catalysts containing earth-abundant elements for the oxygen evolution reaction (OER) in photoelectrochemical (PEC) systems is highly desired for low-cost energy storage and conversion. In this work, mesoporous α-Fe_2O_3 thin film photoanodes coated with manganese oxide ($Mn_3O_{4+\delta}$) co-catalysts are prepared by a dip-coating method. The co-catalyst coating significantly enhances PEC water oxidation performance as compared with the uncoated α-Fe_2O_3. To understand the origin of this enhancement, *in-situ* X-ray absorption spectroscopy is employed to monitor the valence state of Mn in the $Mn_3O_{4+\delta}$ co-catalyst as a function of applied potential. It is found that the enhancement of the photocurrent is governed by the Mn valency, and the most prominent enhancement takes place at the valency of ~3.4+, which is due to the optimal e_g electron filling in Mn cations as the electrocatalyst for OER. Our investigation indicates that the contribution of $Mn_3O_{4+\delta}$ co-catalyst to OER kinetics is variable at different applied potentials.

KEYWORDS: *manganese oxide, co-catalyst, photoanode, hematite, valency*

INTRODUCTION

The rapid increase of human population has resulted in an ever-growing demand for energy. This has led to researchers seeking for new alternative sustainable energy solutions to produce energy for the continual economic growth. Photoelectrochemical (PEC) water splitting, which directly utilizes solar energy to split water into H_2 and O_2, is one of the most attractive strategies for producing hydrogen fuel. Over the years, numerous water splitting PEC devices using different metal oxide photoanodes such as TiO_2,[1,2] WO_3,[3,4] $BiVO_4$,[5,6] and Fe_2O_3[7,8] have been developed.[9,10] Among them, hematite (α-Fe_2O_3) has been found to be a promising photo-anode for oxygen evolution reaction (OER) because of its low bandgap[11] (E_g = 2.1 eV) for visible light absorption, relatively high chemical stability, and low cost. However, the pristine α-Fe_2O_3 only achieves a fraction of its theoretical current density, which is mainly due to the low carrier mobility (<10^{-1} cm^2 V^{-1} s^{-1}), short-hole diffusion length (2~4 nm), and short photogenerated charge carrier lifetime (~10 ps).[12-14] All of these factors result in a high charge recombination rate within the bulk α-Fe_2O_3, significantly inhibiting the number of charge carriers generated at the semiconductor-electrolyte interface for OER.

To overcome this challenge, α-Fe_2O_3 has been nanostructured into mesoporous structures,[15-17] which not only increases the probability for the holes to reach the semiconductor-electrolyte interface, but also improves the α-Fe_2O_3 light absorption.[18] Unfortunately, the maximum current density of α-Fe_2O_3 is still interior to the theoretical value of 12 mA cm^{-2}. Also, due to the slow kinetics of α-Fe_2O_3 for water oxidation, the onset potential of α-Fe_2O_3 under illumination is lower than the expected value. To further boost its PEC performance, efforts have been devoted to coupling mesoporous Fe_2O_3 with co-catalysts, such as IrO_2,[19,20] MnO_x,[21] $Co(OH)_2$,[22] FeB,[23] and N-doped carbon dots.[24] These co-catalysts are usually coated on the Fe_2O_3 photoanode and directly contact with the electrolyte. They are able to promote the OER reaction kinetics electro-chemically and result in enhanced water oxidation performance.[25,26]

Among various co-catalysts, manganese oxides are one of the most attractive due to their low cost and low toxicity. Previous studies[27,28] have investigated the light-harvesting efficiency, photo-conversion ability, surface treatment effects, charge injection rate, and etc. on various MnO_x/α-Fe_2O_3 photoanodes. In general, coating a layer of MnO_x co-catalyst has improved the performance of α-Fe_2O_3 photoanode. However, conversely, it was also reported that the MnO_x coating could suppress the hematite's photocurrent.[21] It has also been reported that the Mn cations with Mn^{3+} valence state exhibit best electrocatalytic activity towards OER.[29] To resolve these conflicting reports, it is necessary to

conduct in operando studies on the valency of Mn in the manganese oxide co-catalyst modified α-Fe$_2$O$_3$ photoanode. It is expected that such measurements help to reveal the function of the manganese oxide co-catalyst in α-Fe$_2$O$_3$ photoanodes. To our best of knowledge, this effort has not been reported to date.

In this work, we investigate the valence state of Mn at various potential steps in Mn$_3$O$_{4+\delta}$ co-catalyst modified mesoporous α-Fe$_2$O$_3$ thin film (denoted as Mn$_3$O$_{4+\delta}$-Fe$_2$O$_3$). The optimization of coating thickness of the Mn$_3$O$_{4+\delta}$ co-catalyst layer was firstly conducted. Then, with the aid of *in-situ* X-ray absorption spectroscopy, the valence state of Mn in Mn$_3$O$_{4+\delta}$ at various potentials is correlated to the photocurrent. This work provides a new sight into the understanding of Mn$_3$O$_{4+\delta}$ co-catalyst in PEC water oxidation.

EXPERIMENTAL SECTION

Preparation of α-Fe$_2$O$_3$ electrode. The preparation procedure of α-Fe$_2$O$_3$ electrode is shown in Figure S1. First, the α-Fe$_2$O$_3$ nanoarrays were prepared via an electrodeposition method, which was conducted in a customized three-electrode glass cell. The electrolyte was an aqueous solution containing 0.050 M FeCl$_2$, 0.025 M Na$_2$SO$_4$ and 0.010 M CH$_3$OONa. The Ag/AgCl electrode (filled with saturated KCl solution) and Pt wire served as the reference and counter electrode, respectively. To deposit the β-FeOOH film onto the FTO glass, the potential was held at 1.2 V vs. Ag/AgCl for 1 hr. The electrodeposition reaction was conducted at 70 °C, which was maintained by a water bath. The resultant β-FeOOH electrode was annealed in air at 550 °C for 4 h with a heating rate of 5 °C/min. Before cooling down, it was further calcinated at 800 °C in air for 20 min with a heating rate of 10 °C/min to give the mesoporous α-Fe$_2$O$_3$ electrode.

Fabrication of Mn$_3$O$_{4+\delta}$-Fe$_2$O$_3$ electrode. Mn(acac)$_3$ (manganese (III) acetylacetonate), TOPO (trioctylphosphine oxide) and HAD (1-hexadecylamine) were pr e-dissolved in hexane and the mixture was ultrasonicated to form homogeneous light-brown color solution. Then the as-prepared Fe$_2$O$_3$ mesoporous electrode was immersed in the as-prepared Mn-precursor solution for 30 min. Subsequently, the FTO substrate was removed from the dip-coating solution and washed with hexane before it was annealed at 270 °C in argon for 30 min with a heating rate of 5 °C/min. As-produced Mn$_3$O$_{4+\delta}$-coated α-Fe$_2$O$_3$ electrode was denoted as Mn$_3$O$_{4+\delta}$-Fe$_2$O$_3$ electrode.

Materials characterization. The morphologies were characterized by both field emission scanning electron microscope (FESEM, JEOL 6340) and transmission electron microscope (TEM) (JEOL 2010, 200 kV). Thin film X-ray diffraction (XRD) patterns were collected by Shimadzu LabX-XRD-6000 (Cu Kα radiation, $\lambda = 1.5418$ Å) with 2θ ranging from 10° to 80°. Ultraviolet-visible (UV–vis) absorption spectra of the samples were recorded using an UV–vis–NIR spectrophotometer (PerkinElmer, Lambda 750S). X-ray photoelectron spectroscopy (XPS) was conducted at the Singapore Institute of Manufacturing Technology (SIMTech), A*STAR. X-ray absorption near edge structure (XANES) was measured at XAFCA beamline of Singapore Synchrotron Light Source (SSLS).

In-situ XANES characterization. *In-situ* XANES experiments were carried out at the SSLS XAFCA beamline. The X-ray beam energy was calibrated using the Fe metal foil K edge at 7.112 keV. A Si (111) double-crystal monochromator was employed to reduce the harmonic content of the monochrome beam. *In-situ* XANES testing was performed in 1.0 M NaOH electrolyte with a three-electrode electrochemical cell as PEC characterization under argon atmosphere. All data were collected in fluorescence mode under applied potential from 0.5 V to 1.8 V vs. RHE controlled by a CHI 660E electrochemical workstation. For each Mn$_3$O$_{4+\delta}$-Fe$_2$O$_3$ sample, *in-situ* XANES spectra were recorded on Mn and Fe K edges under illumination by simulating solar irradiation source. The XANES edge position is used to determine the valency based on standard reference materials with known valency. The metallic Fe foil, Cu foil as well as Fe$_2$O$_3$, MnO,

Mn$_2$O$_3$, MnO$_2$ standards (prepared via squash method) were employed as references. Data analysis was performed with the Athena software package.

PEC Characterization. Photoelectrochemical (PEC) measurements were carried out on CHI 660E electrochemical work station (CH Instruments, Inc.). PEC testing was performed in 1.0 M NaOH (pH = 13.6) electrolyte with a three-electrode electrochemical cell. A Hg/HgO electrode (filled with 1.0 M NaOH) and a graphite rod served as the reference electrode and counter electrode, respectively. The as-prepared working electrodes have a geometric surface area of 0.28 cm². The light source was illumination from a 150 W xenon solar simulator (67005, Newport Corp.) through a solar (KG 3) filter, with a measured intensity equivalent to standard AM1.5 sunlight (100 mW cm^{-2}) at the sample surface. Electrochemical impedance spectroscopy (EIS) measurements were carried out using an automated potentiostat (Methrohm–Autolab, AUT 83285) with the same three-electrode electrochemical cell. The EIS data was collected at the open circuit potential with a voltage perturbation of 50 mV and the frequency ranges from 100 kHz to 0.1 Hz. The typical Mott–Schottky plot was extracted at 10 kHz.

RESULTS AND DISCUSSION

Mn$_3$O$_{4+\delta}$-Fe$_2$O$_3$ was prepared by the dip-coating method as shown in Figure S1. The crystal structure and phase purity of α-Fe$_2$O$_3$ and Mn$_3$O$_{4+\delta}$-Fe$_2$O$_3$ were examined by XRD (Figure 1c), and the morphology evolution was monitored by SEM (Figure 1a and 1b). In the first step, the electrochemical deposition gives edge-exposed β-FeOOH nanoplates (Figure S2),[30] which have a width of ~550 nm and an edge thickness of ~50 nm. From the cross-section view (inset, Figure S2), it can be seen that the film thickness is ~1.2 μm. Upon annealing at 800 °C, the electrochemical-deposited β-FeOOH nanoplates undergo dehydroxylation, transforming into mesoporous α-Fe$_2$O$_3$ (Figure 1a). The XRD pattern of Fe$_2$O$_3$ (Figure 1c) is indexed to the rhombohedral corundum phase of α-Fe$_2$O$_3$, with the lattice parameters of a = b = 5.0357 Å and c = 13.7489 Å (JCPDS 33-0664). This is further confirmed by the TEM observation (Figure 1e), where the d spacing of 0.503 nm corresponds to the (100) plane of α-Fe$_2$O$_3$. To coat with the manganese oxide co-catalyst layer, the as-prepared mesoporous α-Fe$_2$O$_3$ was dipped into a Mn(acac)$_3$/TOPO/HAD solution and subsequently annealed at 270 °C to produce mesoporous Mn$_3$O$_{4+\delta}$-Fe$_2$O$_3$. In this recipe, TOPO serves as the capping agent to prevent particles from agglomeration and HAD is the reducing agent to reduce Mn^{3+} partially to Mn^{2+}. By comparing the XRD patterns of Mn$_3$O$_{4+\delta}$-Fe$_2$O$_3$ and Fe$_2$O$_3$, it is observed that their diffraction peaks are almost the same, without the detection of the manganese oxide peaks. This indicates that the thickness of the manganese oxide coating layer is quite small and the modification is only limited to the surface of α-Fe$_2$O$_3$ without altering the bulk crystal structure of the matrix. With the dip-coating method, manganese oxide can be clearly observed on the mesoporous α-Fe$_2$O$_3$ surface in energy-dispersive X-ray spectroscopy (EDS) mapping by SEM (Figure 1b). Note that the mesoporous film is highly desirable because it not only increases the surface area of electrode, but also enhances the charge transfer at the semiconductor-electrolyte interface for better PEC performance.[7,31]

After dipping-and-coating manganese oxide onto the α-Fe$_2$O$_3$, we probe the structure of the final product and it is concluded that the manganese oxide coated on α-Fe$_2$O$_3$ is Mn$_3$O$_4$ spinel oxide with cation vacancies (denoted as Mn$_3$O$_{4+\delta}$). In the high resolution TEM (HRTEM) image of

1
2
3
4
5
6
7
8
9
10
11
12
13
14
15
16
17
18
19
20
21
22
23
24
25
26
27
28
29
30
31
32
33
34
35
36
37
38
39
40
41
42
43
44
45
46
47
48
49
50
51
52
53
54
55
56
57
58
59
60

$Mn_3O_{4+\delta}$-Fe_2O_3 (Figure 1f), the lattice spacing of 0.250 nm is indexed to the (211) plane distance of Mn_3O_4. This is consistent with the control experiment, where pure Mn_3O_4 was synthesized by the same method in the absence of Fe_2O_3. The resulting XRD pattern (Figure S9B) perfectly matches the standard Mn_3O_4, demonstrating that the manganese oxide synthesized by this recipe is Mn_3O_4.
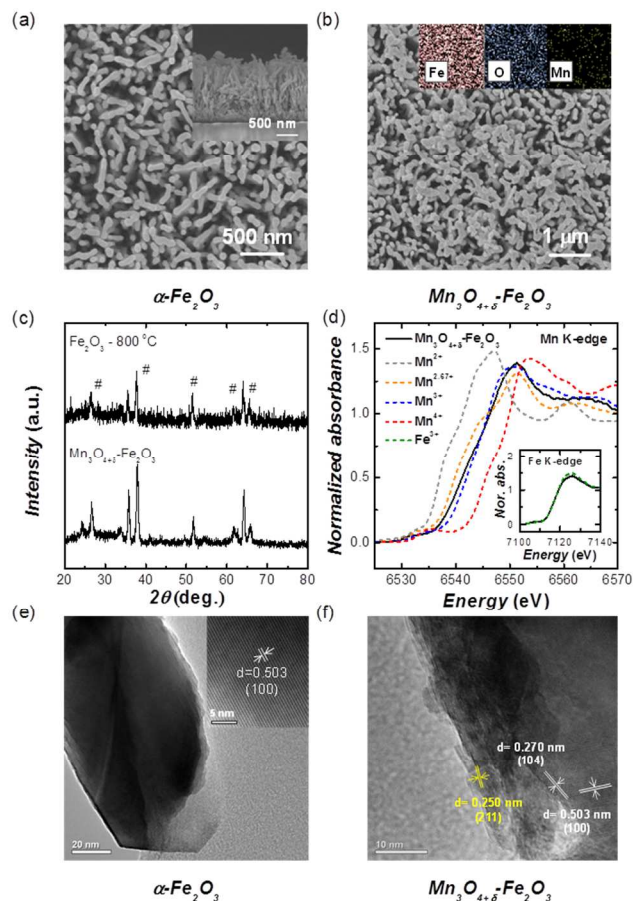

Figure 1. (a) SEM images of α-Fe_2O_3 prepared by annealing β-FeOOH at 800 °C. The inset is the cross-section. (b) SEM images of $Mn_3O_{4+\delta}$-Fe_2O_3. The inset is the corresponding EDS results. (c) XRD patterns of as-prepared α-Fe_2O_3 and $Mn_3O_{4+\delta}$-Fe_2O_3. The FTO peaks are marked as #. (d) XANES spectra of $Mn_3O_{4+\delta}$-Fe_2O_3 at Mn K-edge and Fe K-edge (inset). The dashed lines are MnO, Mn_3O_4, Mn_2O_3, MnO_2 and Fe_2O_3 (inset) standard samples. (e) TEM images of α-Fe_2O_3. Inset is the HRTEM image of α-Fe_2O_3. (f) TEM images of $Mn_3O_{4+\delta}$-Fe_2O_3.

In the XANES result (Figure 1d), the edge position of $Mn_3O_{4+\delta}$-Fe_2O_3 at Mn K-edge indicates a Mn valency of ~+2.75. It is slightly higher than the value (+2.67) of stoichiometric Mn_3O_4. However, the non-stoichiometry in our study is due to the extremely small thickness of Mn_3O_4 coating layer, which usually gives various defects such as cation vacancy. This agrees well with the previous study, where the oxidation degree (the ratio of Mn^{3+} to Mn^{2+}) of Mn_3O_4 could be varied between 2.05 and 3.04.[32] Therefore, the MnO_x coated on α-Fe_2O_3 indeed presents in the forms of $Mn_3O_{4+\delta}$ (δ = 0.125), which has the same crystal structure as Mn_3O_4 but different Mn valency. In the case of Fe, the edge position of $Mn_3O_{4+\delta}$-Fe_2O_3 at Fe K-edge overlaps with Fe_2O_3 standard (inset, Figure 1d), indicating the unchanged bulk crystal structure of Fe_2O_3 after dip-coating reaction.

The thin layer of $Mn_3O_{4+\delta}$ coated on α-Fe_2O_3 film was then examined for PEC performance under dark and light conditions. Figure 2a shows the photocurrent-time curves of α-Fe_2O_3 and $Mn_3O_{4+\delta}$-Fe_2O_3 under chopped illumination in 1.0 M NaOH at 1.1 V and 1.3 V vs. RHE. The photocurrent density of $Mn_3O_{4+\delta}$-Fe_2O_3 (0.52 mA cm^{-2} at 1.3 V vs. RHE) is ~2.8 times higher than α-Fe_2O_3 (0.18 mA cm^{-2} at 1.3 V vs. RHE), demonstrating that the manganese oxide coating layer on α-Fe_2O_3 efficiently improved the PEC activity. Note here that the current density is by geometry area of the anode with the assumption that the thin coating layer of $Mn_3O_{4+\delta}$ does not change the surface roughness of α-Fe_2O_3 anode. The enhanced PEC OER activity at $Mn_3O_{4+\delta}$-Fe_2O_3 is also proved by the faster O2 generation quantified by gas chromatograph (Figure S17).
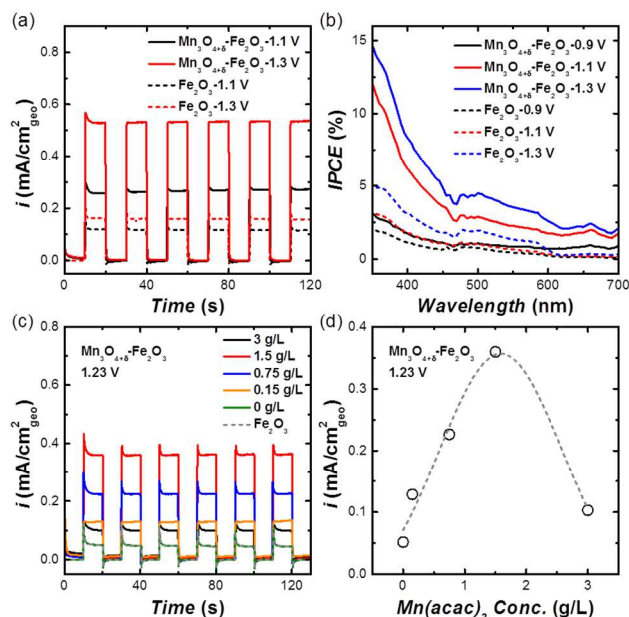

Figure 2. (a) I–t curves recorded with chopped AM1.5G illumination of Fe_2O_3 and $Mn_3O_{4+\delta}$-Fe_2O_3 samples at 1.1 and 1.3 V vs. RHE in 1.0 M NaOH electrolyte. The current density is normalized to the geometric surface area of the FTO electrode. (b) IPCE of Fe_2O_3 and $Mn_3O_{4+\delta}$-Fe_2O_3 at 0.9, 1.1, and 1.3 V vs. RHE. (c) Chopped I–t curves of $Mn_3O_{4+\delta}$-Fe_2O_3 prepared with various concentrations of $Mn(acac)_3$. The current density was collected at 1.23 V vs. RHE in 1.0 M NaOH electrolyte and normalized to the geometric surface area of the FTO electrode. (d) PEC activity of $Mn_3O_{4+\delta}$-Fe_2O_3 as a function of the concentration of $Mn(acac)_3$. PEC activity is defined as the current density at 15th second after light on in the I-t curve of panel (c).

To estimate the efficiency of the water oxidation process, the incident photon to current efficiency (IPCE) curves of α-Fe_2O_3 and $Mn_3O_{4+\delta}$-Fe_2O_3 at different potentials are shown in Figure 2b. It can be seen that the $Mn_3O_{4+\delta}$-Fe_2O_3 sample exhibited higher efficiency than α-Fe_2O_3 at each potential. For example, at 1.3 V vs. RHE, the IPCE of $Mn_3O_{4+\delta}$-Fe_2O_3 at 420 nm is 7%, while the Fe_2O_3 is only 3%. The poor IPCE of pure α-Fe_2O_3 can be ascribed to rapid surface charge recombination, especially in the visible light region.[33] The photoresponse of α-Fe_2O_3 has dropped to almost zero (i.e., IPCE < 0.5% at 610 nm) at wavelengths longer than 610 nm. In contrast, $Mn_3O_{4+\delta}$-Fe_2O_3 still shows a prominent photo-response at this wavelength region (> 610 nm). The higher IPCE of $Mn_3O_{4+\delta}$-Fe_2O_3 throughout the visible light region suggests that the presence of $Mn_3O_{4+\delta}$-coating not only increases the

possibility of carrier migration, but also facilitates the utilization of carriers at low-energy-input region. Note that the IPCE efficiencies of both $Mn_3O_{4+\delta}$-Fe_2O_3 and α-Fe_2O_3 are not among the top,[7,14,34] which is possibly due to the inherent recombination of charges in bulk or at the semiconductor/electrolyte interface. By comparing the APCE (absorbed photon to current conversion efficiency) of $Mn_3O_{4+\delta}$-Fe_2O_3 and Fe_2O_3, it shows the same trend as observed in IPCE (Figure S10), indicating the excellent efficiency of charge separation and collection at $Mn_3O_{4+\delta}$-Fe_2O_3.[35]

Hereby, our results demonstrate that the PEC performance of α-Fe_2O_3 is significantly enhanced by $Mn_3O_{4+\delta}$-coating. The enhancement can be attributed to two reasons. First, since the CB (conduction band) of $Mn_3O_{4+\delta}$ locates at a more negative position than α-Fe_2O_3, photo-excited electron in the CB of $Mn_3O_{4+\delta}$ would be transferred to α-Fe_2O_3, which greatly improves its charge separation and leads to the enhanced PEC performance (Figure S11). Second, considering the fact that $Mn_3O_{4+\delta}$ possesses excellent electrochemical OER performance,[36,37] $Mn_3O_{4+\delta}$-coating served as the co-catalyst that more efficiently utilizes the carriers provided by α-Fe_2O_3. This is conceptually in analogous to the application of IrO_2 and RuO_2 co-catalysts to photoanodes.[38-40]

To reveal the physical origin of the improved PEC performance on $Mn_3O_{4+\delta}$-Fe_2O_3, we first characterized the band gap by visible light absorption in UV-vis spectroscopy. In Figure S12A, $Mn_3O_{4+\delta}$-Fe_2O_3 exhibited higher edge position (~640 nm) than Fe_2O_3 (~600 nm). This red-shift of absorption wavelength at $Mn_3O_{4+\delta}$/α-Fe_2O_3 indicates the stronger capability of absorbing solar energy,[41] thus improving the photochemical performance. Moreover, according to the edge position of UV-vis absorption, the band gap of $Mn_3O_{4+\delta}$-Fe_2O_3 is quantified as 1.93 eV and that of α-Fe_2O_3 is 2.07 eV. The smaller band gap of $Mn_3O_{4+\delta}$-Fe_2O_3 indicates its more efficient separation of photo-generated electron-hole pairs,[42,43] which greatly enhances the photochemical activity. The $Mn_3O_{4+\delta}$ with cation vacancy is ascribed to p-type semiconductor and the pristine α-Fe_2O_3 is considered as a n-type semiconductor.[7] Hence, the internal electric field could form at the interface of $Mn_3O_{4+\delta}$/Fe_2O_3,[44] and we therefore postulate that this internal electric field within the $Mn_3O_{4+\delta}$/Fe_2O_3 probably accelerates the separation of electron-hole pairs. The presence of this internal electric field can be supported by the observation that either the pure α-Fe_2O_3 or the pure Mn_3O_4 possesses poorer PEC performance than $Mn_3O_{4+\delta}$-Fe_2O_3 under visible light irradiation (Figure 2 and S9).

Another factor that governs the PEC performance is the charge transfer property, which was studied by electrochemical impedance spectroscopy (EIS) measure-ments and correlated with the PEC activity. In the Nyquist plots of Fe_2O_3 and $Mn_3O_{4+\delta}$-Fe_2O_3 (Figure S12), both Fe_2O_3 and $Mn_3O_{4+\delta}$-Fe_2O_3 showed semicircles in high frequency region and a linear tail in low frequency region in dark and light conditions. The semicircle in high frequency region is ascribed to the combination of charge transfer resistance, and the linear line in the low frequency region reflects the diffusion process.[45] The radius of α-Fe_2O_3 in high frequency region does not show good asemicircle property (Figure S12B) because of the absence of charge carriers. The similarity of the linear behaviors of α-Fe_2O_3 in dark and light conditions illustrates the poor separation of electrons and holes in bulk α-Fe_2O_3 electrode, which is due to the lack of the driving force at the open cir-

cuit potential. Compared with α-Fe_2O_3, the semicircle of $Mn_3O_{4+\delta}$-Fe_2O_3 is smaller, which reflects the higher interfacial charge transfer rate across the electrode-electrolyte interface. To quantify the EIS data, the solution resistance (R_s), charge transfer resistance (R_{ct}), immediate adsorption resistance (R_{ads}), immediate adsorption capacitance (C_{ads}), interface capacitance (C_c) and Warburg impedance (Z_w) were fitted into the equivalent circuit (Figure S12B) and the as-obtained values were listed in Table S3. Compared with α-Fe_2O_3, $Mn_3O_{4+\delta}$-Fe_2O_3 possesses a lower R_{ct} and higher C_c, indicating that the presence of $Mn_3O_{4+\delta}$-coating improves the electron transfer rate.[46] Moreover, based on the intercept of Mott-Schottky plot (Figure S12D), the flat band potential (E_{fb}) of α-Fe_2O_3 is estimated to be 0.30 V and $Mn_3O_{4+\delta}$-Fe_2O_3 is 0.25 V. The lower E_{fb} of $Mn_3O_{4+\delta}$-Fe_2O_3 indicates a higher fermi level and a higher electronic energy level, leading to the enhancement of photocatalytic activity.[47] Another parameter, the donor density, can be extracted from the slope of Mott-Schottky plot. The slope of $Mn_3O_{4+\delta}$-Fe_2O_3 curve is apparently smaller than Fe_2O_3, indicating that the transition of majority carriers at $Mn_3O_{4+\delta}$-Fe_2O_3 is much easier. As evidenced by the systematic EIS study, the excellent charge transfer property of $Mn_3O_{4+\delta}$-Fe_2O_3 is experimentally demonstrated as a physical parameter that leads to the high PEC activity, which is possibly due to the formation of the $Mn_3O_{4+\delta}$/Fe_2O_3 interface in $Mn_3O_{4+\delta}$-Fe_2O_3.

The importance of the $Mn_3O_{4+\delta}$/Fe_2O_3 interface is also verified by the relationship between the PEC performance and the coating amount of $Mn_3O_{4+\delta}$-layer, which is varied by tuning the concentration of $Mn(acac)_3$ during the dip procedure. To probe the coating amount of $Mn_3O_{4+\delta}$, we employed XPS technique (Figure S13) to quantify the surface Mn content. It should be noted that PEC OER catalysis is essentially a surface process, where only the surface or near-surface region interacts with oxygenated species.[48] Therefore, to have a more direct understanding of the structure-performance relationship, we aim to use XPS to reveal the surface information of our photoelectric catalysts. The XPS results show that with the increasing $Mn(acac)_3$ concentration, the increasing Mn content was observed (Table S2), which proves that more $Mn_3O_{4+\delta}$ had been deposited on the α-Fe_2O_3 matrix. The unchanged Mn 2p and Fe 2p peaks of different $Mn_3O_{4+\delta}$-coating amount (Figure S13) further demonstrate that the basic structure of the Mn/Fe-component remains the same,[45] but only the $Mn_3O_{4+\delta}$ amount is varied. Figure 2c is the I-t curves of $Mn_3O_{4+\delta}$-Fe_2O_3 prepared with different Mn-precursor concentration, ranging from 0 to 3 g/L. To examine the effect of $Mn_3O_{4+\delta}$-coating amount, the PEC activity is defined as the current density at 15th second of the I-t curve (Figure 2c) and plotted as a function of $Mn(acac)_3$ concentration. As shown in Figure 2d, the volcano-shaped relationship indicates that the $Mn_3O_{4+\delta}$/Fe_2O_3 interface gives the best performance at ~1.5 g/L. On the left branch of the volcano trend (Figure 2d), the amount of $Mn_3O_{4+\delta}$-coating should be high enough to trigger the passivation of the surface traps and also the formation of the hole acceptor on the Fe_2O_3 surface, which can improve the kinetics of the OER. However, on the right branch, further increasing the concentration of Mn-precursor (beyond ~1.5 g/L) results in the formation of a too thick $Mn_3O_{4+\delta}$-layer above Fe_2O_3, which blocks the hole transport to the topmost $Mn_3O_{4+\delta}$ surface and weakens the contact between the $Mn_3O_{4+\delta}$ surface and the $Mn_3O_{4+\delta}$/Fe_2O_3 interface. It is worth

noting that with the optimized $Mn_3O_{4+\delta}$-coating amount, the PEC activity ranks among top of the popular metal oxide PEC catalysts (Table S4).

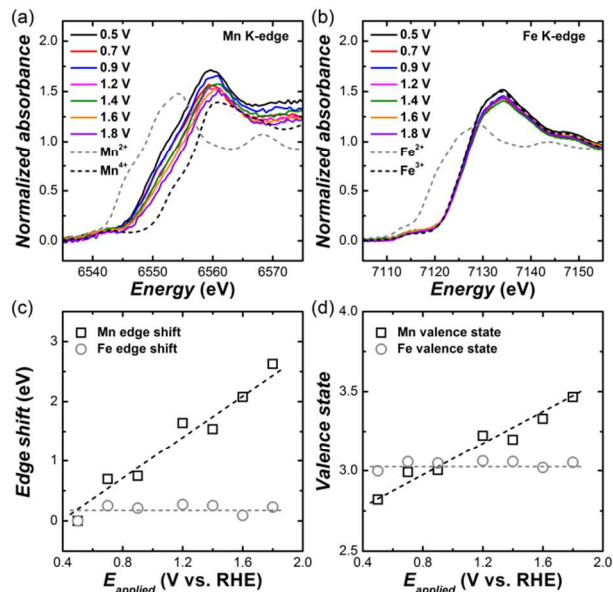**Figure 3.** *In-situ* (a) Mn and (b) Fe K-edge XANES spectra of $Mn_3O_{4+\delta}$-Fe_2O_3 with the applied potential from 0.5 to 1.8 V *vs.* RHE in 1.0 M NaOH under light illumination. Applied potential induced (c) the variation of K-edge and (d) valence states of Mn and Fe under light illumination.

Since α-Fe_2O_3 locates in the interior of $Mn_3O_{4+\delta}$-Fe_2O_3 film (away from the solid-liquid interface), $Mn_3O_{4+\delta}$ is considered as the catalyzing center that directly interacts with oxygenated species in OER. To further understand the active site under photoelectrochemical reaction condition, *in-situ* XANES was performed to study the Mn structural change. From 0.5 to 1.8 V *vs.* RHE with light illumination, the edge position of Mn K-edge gradually shifts to the high-energy region (Figure 3a), indicating an increasing oxidation state of Mn. This *in-situ* XANES photoelectrochemical observation is analogous to the previous *in-situ* XANES electrochemical studies on pure manganese oxides, where an increase of the applied potential leads to the increasingly oxidized Mn.[36,49,50] In contrast, the position of Fe K-edge remains unchanged with various applied potentials (Figure 3b), indicating that the valence state of Fe keeps unchanged (which may be due to the thick α-Fe_2O_3 layer). In order to quantify the valency variation, we employ the integral method[50] to determine the edge position (Figure 3c), which is further translated into the valence state (Figure 3d). It can be seen that the Mn valency varies between +2.8 and +3.5, while Fe remains at +3.0.

The Mn valency of +3.5 at 1.8 V *vs.* RHE (Figure 3d) strongly indicates that the PEC catalysis of oxygen evolution at $Mn_3O_{4+\delta}$-Fe_2O_3 relies on the Mn^{3+}/Mn^{4+} pairs. It indicates that the role of the $Mn_3O_{4+\delta}$ co-catalyst can reach maximum at the high potential. The enhanced photocurrent at high potential region is mainly from the electrocatalyst role of the $Mn_3O_{4+\delta}$ co-catalyst layer. This finding is analogous to the land mark study, where the Mn^{3+}/Mn^{4+} oxide is the phase pertinent to the observed electrochemical OER activity at 1.8V *vs.* RHE.[36] With advancement, our work broadens. The potential window and features the Mn valency during the PEC catalysis. Even though the starting manganese oxide is

totally different from that previously,[36] the universal role of Mn^{3+}/Mn^{4+} pair as the active site in either electrochemical or photoelectrochemical performance is demonstrated here.
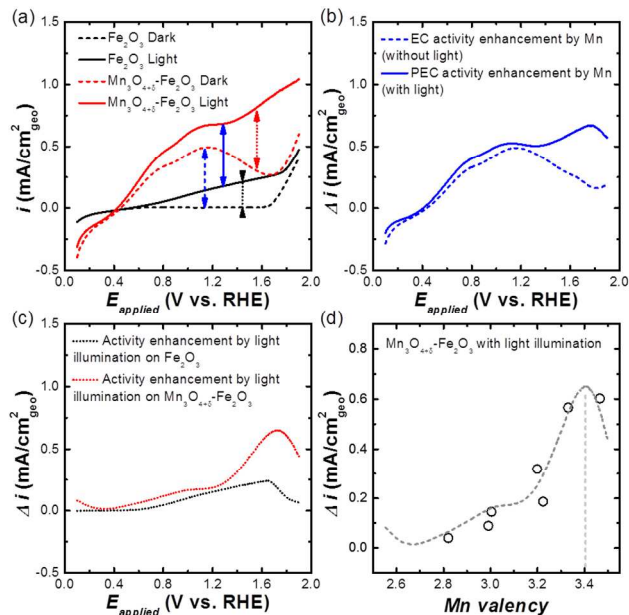

Figure 4. (a) LSV curves of Fe_2O_3 and $Mn_3O_{4+\delta}$-Fe_2O_3 collected with and without light illumination under the scan rate of 100 mV/s in 1.0 M NaOH. (b) The PEC activity contribution of Mn-coating as a function of Mn valency. (c) The activity enhancement contributed by light illumination on Fe_2O_3 and $Mn_3O_{4+\delta}$-Fe_2O_3. (d) The Δi of $Mn_3O_{4+\delta}$-Fe_2O_3 as a function of Mn valence state.

To further understand the role of $Mn_3O_{4+\delta}$ as the photoelectrochemical OER co-catalyst, the Mn valency variation probed by *in-situ* XANES and LSV curves are combined. First, the gap between the LSV curve of α-Fe_2O_3 Dark and $Mn_3O_{4+\delta}$-Fe_2O_3 Dark (Figure 4a) indicates the role of manganese oxide coating as the electrochemical catalyst. As shown in Figure 4b, at the region higher than the OER onset potential (~1.6 V *vs.* RHE), the Δi is larger than zero, which indicates that the manganese oxide coating is a better electrochemical OER catalyst than α-Fe_2O_3. This observation supports our statement that $Mn_3O_{4+\delta}$-coating serves as the co-catalyst that more efficiently utilizes the charge provided by α-Fe_2O_3, and thus gives better PEC performance. It is worth noting that the current density of $Mn_3O_{4+\delta}$-Fe_2O_3 LSV curves (within 0.5 V~1.4 V) is largely contributed by the electrochemical capacitance of manganese oxide, which has been observed in previous landmark works.[36,51] Second, the gap between the LSV curve of the same material collected with light and without light reflects the OER activity induced by illumination. In Figure 4c, by comparing this gap on α-Fe_2O_3 and $Mn_3O_{4+\delta}$-Fe_2O_3, we studied the photoelectro-catalytic activity of $Mn_3O_{4+\delta}$-coating at different potential. Below 1.2 V *vs.* RHE, the two curves almost overlap with each other, which means that at this potential window, with $Mn_3O_{4+\delta}$ co-catalyst, the PEC activity enhancement is negligible. At the potential higher than 1.2 V *vs.* RHE, the Δi of $Mn_3O_{4+\delta}$-Fe_2O_3 becomes increasingly larger than α-Fe_2O_3, and reaches the highest value at 1.7 V *vs.* RHE. This suggests that $Mn_3O_{4+\delta}$ co-catalyst starts promoting the PEC catalysis since 1.2 V *vs.* RHE, and the resulting activity enhancement is different at various potentials. Because the increasing potential linearly increases Mn valency (Figure 3d), we propose that various

activity enhancement (Δi) is due to the varied Mn valency. By translating the potential to the corresponding Mn valency, the Δi of $Mn_3O_{4+\delta}$-Fe_2O_3 is plotted as a function of the Mn valence state (Figure 4d). It is observed that the Mn valency with the value lower than +3 contributes poorly; increasing the valence state gives larger Δi and the optimum (highest Δi) takes place at $Mn^{3.4+}$ (Figure 4d). This trend elucidates the role of $Mn_3O_{4+\delta}$-coating as the photoelectrochemical OER co-catalyst at different potential window: the utilization of light is governed by the Mn valence state and the $Mn^{3.4+}$ takes the fullest advantage of the light illumination.

CONCLUSION

In summary, the mesoporous α-Fe_2O_3 coated by ultrathin $Mn_3O_{4+\delta}$ co-catalyst showed enhanced photoelectrochemical OER performance to pristine α-Fe_2O_3. Compared with the PEC activity of pristine α-Fe_2O_3 (0.18 mA cm^{-2} at 1.3 V *vs.* RHE), the higher photocurrent generated by the $Mn_3O_{4+\delta}$-Fe_2O_3 (~0.52 mA cm^{-2}) is attributed to the improved charge separation, the more efficient interfacial charge transfer across the semiconductor-electrolyte interface, and the contribution of the co-catalyst. The higher IPCE of $Mn_3O_{4+\delta}$-Fe_2O_3 indicates the enhanced carrier migration ability and the improved utilization of solar spectrum. The importance of the $Mn_3O_{4+\delta}/Fe_2O_3$ interface on OER was studied by varying the coating amount of $Mn_3O_{4+\delta}$-layer. With the aid of *in-situ* XANES, it was found that at varied potential steps, the $Mn_3O_{4+\delta}$-co-catalyst plays different roles. This is governed by the Mn valence state and the highest enhancement is optimized at $Mn^{3.4+}$. This finding provides a new sight into the understanding of manganese oxide co-catalyst in PEC water oxidation.

ASSOCIATED CONTENT

Supporting Information

The Supporting Information is available free of charge on the ACS Publications website at DOI: XXXXXXX.

Experimental details; further information on the preparation of α-Fe_2O_3; electrochemical characterization of Mn_3O_4 and $Mn_3O_{4+\delta}$-Fe_2O_3; *In-situ* XANES curves and XPS spectra of $Mn_3O_{4+\delta}$-Fe_2O_3 (PDF)

AUTHOR INFORMATION

Corresponding Author

*xuzc@ntu.edu.sg
*jwager@lbl.gov
*joachimloo@ntu.edu.sg

ORCID

Zhichuan J. Xu: 0000-0001-7746-5920
Joel W. Ager: 0000-0001-9334-9751
Joachim S. C. Loo: 0000-0001-5300-1275

Author Contributions

$^{\Delta}$Ying Liu and Chao Wei contributed equally.

Notes
The authors declare no competing financial interests.

ACKNOWLEDGMENT

REFERENCES

(1) Liu, G.; Wang, L.; Yang, H. G.; Cheng, H. M.; Lu, G. Q. M. Titania-Based Photocatalysts—Crystal Growth, Doping and Heterostructuring. *J. Mater. Chem.* **2010**, *20*, 831-843.

(2) Wang, G.; Wang, H.; Ling, Y.; Tang, Y.; Yang, X.; Fitzmorris, R. C.; Wang, C.; Zhang, J.; Li, Y. Hydrogen-Treated TiO_2 Nanowire Arrays for Photoelectrochemical Water Splitting. *Nano Lett.* **2011**, *11*, 3026-3033.

(3) Chakrapani, V.; Thangala, J.; Sunkara, M. K. WO_3 and W_2N Nanowire Arrays for Photoelectrochemical Hydrogen Production. *Int. J. Hydrogen Energy* **2009**, *34*, 9050-9059.

(4) Li, Y.; Zhang, L.; Liu, R.; Cao, Z.; Sun, X.; Liu, X.; Luo, J. $WO_3@\alpha$-Fe_2O_3 Heterojunction Arrays with Improved Photoelectrochemical Behavior for Neutral pH Water Splitting. *ChemCatChem* **2016**, *8*, 2765-2770.

(5) Kim, T. W.; Choi, K. S. Nanoporous $BiVO_4$ Photoanodes with Dual-Layer Oxygen Evolution Catalysts for Solar Water Splitting. *Science* **2014**, *343*, 990-994.

(6) Park, Y.; McDonald, K. J.; Choi, K. Progress in Bismuth Vanadate Photoanodes for Use in Solar Water Oxidation. *Chem. Soc. Rev.* **2013**, *42*, 2321-2337.

(7) Sivula, K.; Le Formal, F.; Graetzel, M. Solar Water Splitting: Progress Using Hematite (α-Fe_2O_3) Photoelectrodes. *ChemSusChem* **2011**, *4*, 432-449.

(8) Mishra, M.; Chun, D. α-Fe_2O_3 as a Photocatalytic Material: A Review. *Appl. Catal. A-Gen.* **2015**, *498*, 126-141.

(9) Sivula, K.; Krol, R. V. D. Semiconducting Materials for Photoelectrochemical Energy Conversion. *Nat. Rev. Mater.* **2016**, *1*, 15010.

(10) Prévot, M. S.; Sivula, K. Photoelectrochemical Tandem Cells for Solar Water Splitting. *J. Phys. Chem. C* **2013**, *35*, 17879-17893.

(11) Pendlebury, S. R.; Barroso, M.; Cowan, A. J.; Sivula, K.; Tang, J.; Graetzel, M.; Klug, D.; Durrant, J. R. Dynamics of Photogenerated Holes in Nanocrystalline α-Fe_2O_3 Electrodes for Water Oxidation Probed by Transient Absorption Spectroscopy. *Chem. Commun.* **2011**, *47*, 716-718.

(12) Cherepy, N. J.; Liston, D. B.; Lovejoy, J. A.; Hongmei, D.; Zhang, J. Z. Ultrafast Studies of Photoexcited Electron Dynamics in γ- and α-Fe_2O_3 Semiconductor Nanoparticles. *J. Phys. Chem. B* **1998**, *102*, 770-776.

(13) Barroso, M.; Pendlebury, S. R.; Cowan, A. J.; Durrant, J. R. Charge Carrier Trapping, Recombination and Transfer in Hematite (α-Fe_2O_3) Water Splitting Photoanodes. *Chem. Sci.* **2013**, *4*, 2724-2734.

(14) Sivula, K.; Zboril, R.; Le Formal, F.; Robert, R.; Weidenkaff, A.; Tucek, J.; Frydrych, J.; Graetzel, M. Photoelectrochemical Water Splitting with Mesoporous Hematite Prepared by a Solution-Based Colloidal Approach. *J. Am. Chem. Soc.* **2010**, *132*, 7436-7444.

(15) Pendlebury, S. R.; Wang, X.; Le Formal, F.; Cornuz, M.; Kafizas, A.; Tilley, S. D.; Graetzel, M.; Durrant, J. R. Ultrafast Charge Carrier Recombination and Trapping in Hematite Photoanodes under Applied Bias. *J. Am. Chem. Soc.* **2014**, *136*, 9854-9857.

(16) Kay, A.; Cesar, I.; Graetzel, M. New Benchmark for Water Photooxidation by Nanostructured α-Fe_2O_3 Films. *J. Am. Chem. Soc.* **2006**, *128*, 15714-15721.

(17) Lei, W.; Chong-Yong, L.; Schmuki, P. Solar Water Splitting: Preserving the Beneficial Small Feature Size in Porous α-Fe_2O_3 Photoelectrodes during Annealing. *J. Mater. Chem. A* **2013**, *1*, 212-215.

(18) Diab, M.; Mokari, T. Thermal Decomposition Approach for the

Formation of α-Fe$_2$O$_3$ Mesoporous Photoanodes and an α-Fe$_2$O$_3$/CoO Hybrid Structure for Enhanced Water Oxidation. *Inorg. Chem.* 2014, 53, 2304-2309.

(19) Tilley, S. D.; Cornuz, M.; Sivula, K.; Graetzel, M. Light-Induced Water Splitting with Hematite: Improved Nanostructure and Iridium Oxide Catalysis. *Angew. Chem. Int. Ed.* 2010, 49, 6549-6552.

(20) Li, W.; He, D.; Sheehan, S. W.; He, Y.; Thorne, J. E.; Yao, X.; Brudvig, G. W.; Wang, D. Comparison of Heterogenized Molecular and Heterogeneous Oxide Catalysts for Photoelectrochemical Water Oxidation. *Energy Environ. Sci.* 2016, 9, 1794-1802.

(21) Yang, X.; Du, C.; Liu, R.; Xie, J.; Wang, D. Balancing Photovoltage Generation and Charge-Transfer Enhancement for Catalyst-Decorated Photoelectrochemical Water Splitting: A Case Study of the Hematite/MnO$_x$ Combination. *J. Catal.* 2013, 304, 86-91.

(22) Wender, H.; Goncalves, R. V.; Dias, C. S. B.; Zapata, M. J. M.; Zagonel, L. F.; Mendonca, E. C.; Teixeira, S. R.; Garcia, F. Photocatalytic Hydrogen Production of Co(OH)$_2$ Nanoparticle-Coated α-Fe$_2$O$_3$ Nanorings. *Nanoscale* 2013, 5, 9310-9316.

(23) Liao, A.; He, H.; Fan, Z.; Xu, G.; Li, L.; Chen, J.; Han, Q.; Chen, X.; Zhou, Y.; Zou, Z. Facile Room-Temperature Surface Modification of Unprecedented FeB Co-catalysts on Fe$_2$O$_3$ Nanorod Photoanodes for High Photoelectrochemical Performance. *J. Catal.* 2017, 352, 113-119.

(24) Huang, X.; Yang, L.; Hao, S.; Zheng, B.; Yan, L.; Qu, F.; Asiri, A. M.; Sun, X. N-Doped Carbon Dots: A Metal-Free Co-catalyst on Hematite Nanorod Arrays toward Efficient Photoelectrochemical Water Oxidation. *Inorg. Chem. Front.* 2017, 4, 537-540.

(25) Zhong, D. K.; Cornuz, M.; Sivula, K.; Graetzel, M.; Gamelin, D. R. Photo-assisted Electrodeposition of Cobalt-Phosphate (Co-Pi) Catalyst on Hematite Photoanodes for Solar Water Oxidation. *Energy Environ. Sci.* 2011, 4, 1759-1764.

(26) Wheeler, D. A.; Wang, G.; Ling, Y.; Li, Y.; Zhang, J. Z. Nanostructured Hematite: Synthesis, Characterization, Charge Carrier Dynamics, and Photoelectrochemical Properties. *Energy Environ. Sci.* 2012, 5, 6682-6702.

(27) Yin, S.; Wang, X.; Mou, Z.; Wu, Y.; Huang, H.; Zhu, M.; Du, Y.; Yang, P. Synergistic Contributions by Decreasing Overpotential and Enhancing Charge-Transfer in α-Fe$_2$O$_3$/Mn$_3$O$_4$/Graphene Catalysts with Heterostructures for Photocatalytic Water Oxidation. *Phys. Chem. Chem. Phys.* 2014, 16, 11289-11296.

(28) Gurudayal; Jeong, D.; Jin, K.; Ahn, H. Y.; Boix, P. P.; Abdi, F. F.; Mathews, N.; Nam, K. T.; Wong, L. H. Highly Active MnO Catalysts Integrated onto Fe$_2$O$_3$ Nanorods for Efficient Water Splitting. *Adv. Mater. Interfaces* 2016, 3, 1600176.

(29) Robinson, D. M.; Go, Y. B.; Mui, M.; Gardner, G.; Zhang, Z.; Mastrogiovanni, D.; Garfunkel, E.; Li, J.; Greenblatt, M.; Dismukes, G. C. Photochemical Water Oxidation by Crystalline Polymorphs of Manganese Oxides: Structural Requirements for Catalysis. *J. Am. Chem. Soc.* 2013, 135, 3494-3501.

(30) Jiao, S.; Xu, L.; Hu, K.; Li, J.; Gao, S.; Xu, D. Morphological Control of α-FeOOH Nanostructures by Electrodeposition. *J. Phys. Chem. C* 2010, 114, 269-273.

(31) Xi, L.; Bassi, P. S.; Chiam, S. Y.; Mak, W. F.; Tran, P. D.; Barber, J.; Loo, J. S. C.; Wong, L. H. Surface Treatment of Hematite Photoanodes with Zinc Acetate for Water Oxidation. *Nanoscale* 2012, 4, 4430-4433.

(32) Kaczmarek, J.; Wolska, E. Cation and Vacancy Distribution in Nonstoichiometric Hausmanite. *J. Solid State Chem.* 1993, 103, 387-393.

(33) Kment, S.; Riboni, F.; Pausova, S.; Wang, L.; Wang, L.; Han, H.; Hubicka, Z.; Krysa, J.; Schmuki, P.; Zboril, R. Photoanodes Based on TiO$_2$ and α-Fe$_2$O$_3$ for Solar Water Splitting—Superior Role of 1D Nanoarchitectures and of Combined Heterostructures. *Chem. Soc. Rev.* 2017, 46, 3716-3769.

(34) Zhong, D. K.; Sun, J.; Inumaru, H.; Gamelin, D. R. Solar Water Oxidation by Composite Catalyst/α-Fe$_2$O$_3$ Photoanodes. *J. Am. Chem. Soc.* 2009, 131, 6086-6087.

(35) Lin, Y.; Zhou, S.; Sheehan, S. W.; Wang, D. Nanonet-Based Hematite Heteronanostructures for Efficient Solar Water Splitting. *J. Am. Chem. Soc.* 2011, 133, 2398-3401.

(36) Gorlin, Y.; Lassalle-Kaiser, B.; Benck, J. D.; Gul, S.; Webb, S. M.; Yachandra, V. K.; Jaramillo, T. F. In Situ X-ray Absorption Spectroscopy Investigation of a Bifunctional Manganese Oxide Catalyst with High Activity for Electrochemical Water Oxidation and Oxygen Reduction. *J. Am. Chem. Soc.* 2013, 135, 8525-8534.

(37) Wei, C.; Feng, Z.; Scherer, G. G.; Barber, J.; Shao-Horn, Y.; Xu, Z. J. Cations in Octahedral Sites: A Descriptor for Oxygen Electrocatalysis on Transition-Metal Spinels. *Adv. Mater.* 2017, 29, 1606800.

(38) Asai, R.; Nemoto, H.; Jia, Q.; Saito, K.; Iwase, A.; Kudo, A. A Visible Light Responsive Rhodium and Antimony-Codoped SrTiO$_3$ Powdered Photocatalyst Loaded with an IrO$_2$ Cocatalyst for Solar Water Splitting. *Chem. Commun.* 2014, 50, 2543-2546.

(39) Janaky, C.; Chanmanee, W.; Rajeshwar, K. On the Substantially Improved Photoelectrochemical Properties of Nanoporous WO$_3$ through Surface Decoration with RuO$_2$. *Electrocatalysis* 2013, 4, 382-389.

(40) Yoo, H.; Oh, K.; Lee, Y. R.; Row, K. H.; Lee, G.; Choi, J. Simultaneous Co-doping of RuO$_2$ and IrO$_2$ into Anodic TiO$_2$ Nanotubes: A Binary Catalyst for Electrochemical Water Splitting. *Int. J. Hydrogen Energy* 2017, 42, 6657-6664.

(41) Li, G.; Zhang, D.; Yu, J. A New Visible-Light Photocatalyst: CdS Quantum Dots Embedded Mesoporous TiO$_2$. *Environ. Sci. Technol.* 2009, 43, 7079-7085.

(42) Bessekhouad, Y.; Robert, D.; Weber, J. V. Bi$_2$S$_3$/TiO$_2$ and CdS/TiO$_2$ Heterojunctions as An Available Configuration for Photocatalytic Degradation of Organic Pollutant. *J. Photoch. Photobio. A* 2004, 163, 569-580.

(43) Zhou, W.; Liu, H.; Wang, J.; Liu, D.; Du, G.; Cui, J. Ag$_2$O/TiO$_2$ Nanobelts Heterostructure with Enhanced Ultraviolet and Visible Photocatalytic Activity. *ACS Appl. Mater. Inter.* 2010, 2, 2385-2392.

(44) Zhang, J.; Wang, T.; Pohl, D.; Rellinghaus, B.; Dong, R.; Liu, S.; Zhuang, X.; Feng, X. Interface Engineering of MoS$_2$/Ni$_3$S$_2$ Heterostructures for Highly Enhanced Electrochemical Overall-Water-Splitting Activity. *Angew. Chem. Int. Ed.* 2016, 55, 6702-6707.

(45) Li, Z.; Luo, W.; Zhang, M.; Feng, J.; Zou, Z. Photoelectrochemical Cells for Solar Hydrogen Production: Current State of Promising Photoelectrodes, Methods to Improve Their Properties, and Outlook. *Energy Environ. Sci.* 2013, 6, 347-370.

(46) Cheng, W.; He, J.; Sun, Z.; Peng, Y.; Yao, T.; Liu, Q.; Jiang, Y.; Hu, F.; Xie, Z.; He, B.; Wei, S. Ni-Doped Overlayer Hematite Nanotube: A Highly Photoactive Architecture for Utilization of Visible Light. *J. Phys. Chem. C* 2012, 116, 24060-24067.
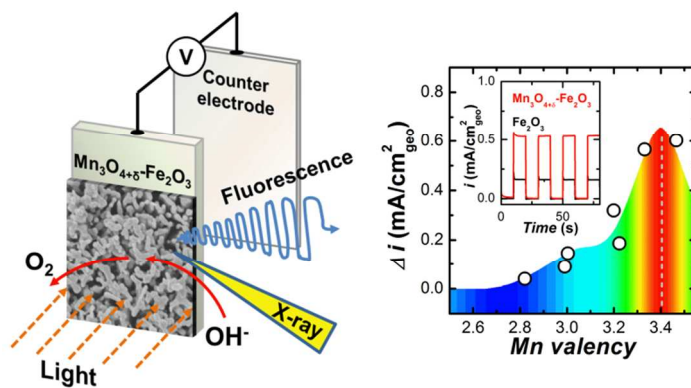
(47) Iandolo, B.; Zhang, H.; Wickman, B.; Zoric, I.; Conibeer, G.; Hellman, A. Correlating Flatband and Onset Potentials for Solar Water Splitting on Model Hematite Photoanodes. *RSC Adv.* 2015, 5, 61021-61030.

(48) Xu, J. Z. From Two-Phase to Three-Phase: The New Electrochemical Interface by Oxide Electrocatalysts. *Nano-Micro Lett.*, 2018, 10, 8.

(49) Risch, M.; Stoerzinger, K. A.; Han, B.; Regier, T. Z.; Peak, D.; Sayed, S. Y.; Wei, C.; Xu, Z.; Shao-Horn, Y. Redox Processes of Manganese Oxide in Catalyzing Oxygen Evolution and Reduction: An In Situ Soft X-ray Absorption Spectroscopy Study. *J. Phys. Chem. C*, 2017, 121, 17682-17692.

(50) Wei, C.; Feng, Z.; Baisariyev, M.; Yu, L.; Zeng, L.; Wu, T.; Zhao, H.; Huang, Y.; Bedzyk, M. J.; Sritharan, T.; Xu, Z. J. Valence Change Ability and Geometrical Occupation of Substitution Cations Determine the Pseudocapacitance of Spinel Ferrite XFe$_2$O$_4$ (X = Mn, Co, Ni, Fe). *Chem. Mater.* 2016, 28, 4129-4133.

(51) Zhou, Y.; Xi, S.; Wang, J.; Sun, S.; Wei, C.; Feng, Z.; Du, Y.; Xu, Z. J. Revealing the Dominant Chemistry for Oxygen Reduction Reaction on Small Oxide Nanoparticles. *ACS Catal.* 2017, 8, 683-691.